

Unified Models of Molecular Emission from Class 0 Protostellar Outflow Sources

J.M.C. Rawlings,^{1*} M.P. Redman² and P.B. Carolan²

¹*University College London, Department of Physics and Astronomy, Gower Street, London WC1E 6BT, United Kingdom*

²*Centre for Astronomy, School of Physics, National University of Ireland Galway, Galway, Ireland*

13 August 2018

ABSTRACT

Low mass star-forming regions are more complex than the simple spherically symmetric approximation that is often assumed. We apply a more realistic infall/outflow physical model to molecular/continuum observations of three late Class 0 protostellar sources with the aims of (a) proving the applicability of a single physical model for all three sources, and (b) deriving physical parameters for the molecular gas component in each of the sources.

We have observed several molecular species in multiple rotational transitions. The observed line profiles were modelled in the context of a dynamical model which incorporates infall and bipolar outflows, using a three dimensional radiative transfer code. This results in constraints on the physical parameters and chemical abundances in each source.

Self-consistent fits to each source are obtained. We constrain the characteristics of the molecular gas in the envelopes as well as in the molecular outflows. We find that the molecular gas abundances in the infalling envelope are reduced, presumably due to freeze-out, whilst the abundances in the molecular outflows are enhanced, presumably due to dynamical activity. Despite the fact that the line profiles show significant source-to-source variation, which primarily derives from variations in the outflow viewing angle, the physical parameters of the gas are found to be similar in each core.

Key words: ISM: molecules – ISM: jets and outflows – ISM: abundances – ISM: kinematics and dynamics – Radiative transfer – Line: profiles

1 INTRODUCTION

The astrophysical mechanism of gravitational infall coupled with rotation and axisymmetric outflows operates on a vast range of scales, ranging from black holes and jets in active galactic nuclei (such as M87), through to high and low mass star formation (Livio 2004) and even brown dwarfs (Whelan et al. 2007).

Searches for the signatures of the early stages of star formation have tended to focus on infall indicators in Class 0 low mass protostellar objects. These possess a luminous protostellar core, but - by definition - most of the mass is contained in a surrounding envelope. In most models the fraction of the mass in the envelope that is infalling increases with time (e.g. Shu, Adams & Lizano 1987). In the early stages the gas is approximately isothermal, and the envelope can be approximated by a spherically symmetric hydrostat-

ically supported cloud. Emission from the envelope includes regions where the gas is infalling and where it is static.

In these circumstances, the classic observational signature of infalling optically thick molecular gas is a double peaked asymmetric line emission profile (Zhou et al. 1993). Molecular emission lines originating from quiescent gas residing in the outer parts of the envelope have linewidths consistent with thermal contributions alone as opposed to thermal and turbulent line broadening of dynamic gas (Keto et al. 2004).

However, collapse seems to almost always lead promptly to disk, jet and (bipolar) outflow formation. These outflows arise because molecular gas in the envelope is entrained by protostellar jets. The latter are hot, high velocity (~ 200 km s^{-1}) jets of mostly atomic hydrogen that carry away excess angular momentum from the core. It is difficult to isolate cases of clouds on the verge of collapse and in such cases local turbulent or global oscillations can mask the weak initial collapse motions (Lada et al. 2003; Redman, Keto & Rawlings

* E-mail: jcr@star.ucl.ac.uk

2006; Gao & Lou 2010). Once collapse is clearly present, line profile shapes become complex and ambiguous. The classic blue-asymmetric line profile shape that can indicate collapse can also be generated by other large scale dynamical effects such as rotation (Redman et al. 2004) or outflows (Rawlings et al. 2004). Moreover, whilst dynamic processes alter spectral line profiles they are also affected by chemical processes which change the molecular abundance, thereby altering the line intensity. These chemical processes include gas-phase reactions, the freeze-out of molecular gas onto dust grains (Schöier et al. 2002) in the cold, dense envelope and the desorption of molecular gas in the warmer outflow regions (Wiseman et al. 2001).

To investigate infall, the presence of other effects should be accounted for. This is not possible with one-dimensional radiative transfer codes because only radial motions can be modelled. Two-dimensional codes are useful because many systems will have cylindrical symmetry around the outflow axis. In fact the line profile observed from a molecular outflow changes dramatically as the angle varies between the outflow axis and the observers line of sight (Ward-Thompson & Buckley 2001). To allow for arbitrary viewing angle relative to the symmetry axis it is therefore necessary to couple the 2D codes to 3D ray-tracing algorithms. Specific sources may exhibit significant deviations from axisymmetry. These could arise, for example, if the outflows are non-axisymmetric and/or there is significant non-symmetric structure in the envelope or circumstellar disk. In these cases a fully three-dimensional approach is required. The drawback of 3D codes is that they have large memory requirements for fine grid resolution.

In this paper, we continue our coupled observational and modelling investigation of early stage collapse objects that are clearly undergoing dynamical activity and harbour a central accreting source. We analyse the emissions from a sample of three low mass protostellar cores which possess evidence of both infall and outflows. The line profiles of several molecular line transitions are observed which effectively probe the conditions in the dense core, diffuse envelope and molecular outflow. These are used to characterise the physical parameters (such as the temperatures, densities and chemical abundances) of each source in the context of a single unified dynamical model that includes infall and a bipolar outflow. To do this we have utilized a 3D radiative transfer code, MOLLIE (MOlecular LIne Explorer, Keto et al. 2004) that is specifically employed to study how the line profiles are constrained by the orientation of the outflow axis with respect to the observer.

We aim to show that a single unified model, comprising a spherically symmetric envelope/inflow and a bipolar outflow with a narrow interface region, can be used to describe the emission from each source. We further wish to test the hypothesis that the significant source-to-source variations that are observed are primarily the results of differences in the source orientation/viewing angle.

Different isotopologues and transitions of the same molecular species preferentially trace somewhat physical different conditions within a dynamically active core. For example, an outflow may be best observed in a low excitation transition of an abundant transition such as ^{12}CO or ^{13}CO line whereas the envelope turbulent velocity may be better constrained by the hyperfine structure in, for example, C^{17}O

lines. The source models were assembled by firstly modelling the different dynamical components, using the transition in which they are most strongly apparent. Then, using this information, a self-consistent model for the entire source was constrained using all species and transitions.

Section 2 summarises the properties of the sources and Section 3 describes our continuum/molecular observations used to constrain the modelling. Section 4 introduces the MOLLIE code and our method, analysis, and the results obtained are given in Section 5. Section 6 discusses these results and our concluding remarks are given in Section 7.

2 SOURCES

Our study concentrates on three protostellar cores; B335, I04166 and L1527, which are each believed to be in the Class 0 phase of evolution for low mass protostellar objects. They have similar spectral energy distributions (SEDs) and, being of a similar evolutionary status, should be described by a single physical model.

Extensive observational data (molecular and continuum) and modelling efforts already exist for these sources and, significantly, spectral signatures of both infall and outflow are seen to be present. We therefore hope to be able to identify the similarities and the source-to-source variations that exist within objects at a similar evolutionary stage.

As an example of the types of variations that are observed, Fig 1 presents the ^{13}CO J=2-1 line profiles at the zero offset (0,0) position for each of the cores. Significant variations in profile shape and strength are clearly evident.

We briefly summarise here the key points from some previous studies, relating to the morphology and dynamical structure of each source.

2.1 B335

B335 is a very well studied core (Hodapp 1998; Wilner et al. 2000; Evans et al. 2005; Stutz et al. 2008; Yen, Takakuwa & Ohashi 2010, 2011) located 250 pc away (Tomita, Saito & Ohtani 1979) and contains the IRAS source 19347 + 0727 (Huard, Sandell & Weintraub 1999).

It is, to a large extent, the prototypical Class 0 infall source in that it was the first such object in which the classic asymmetric double-peaked infall line profiles were identified and analysed (Zhou et al. 1993). This analysis was helped by the facts that it is isolated, singular and approximately spherical. In addition, the outflow lobes are approximately in the plane of the sky; minimising the dynamical confusion between infall and outflows.

The infall component was detected through the observation of several transitions in both single dish and interferometric modes (Chandler & Sargent 1993; Zhou et al. 1993; Velusamy, Kuiper, & Langer 1995; Nisini et al. 1999). The clear presence of infall, coupled with the existence of a massive envelope gas indicates significant accretion and is consistent with a Class 0 protostellar object (André, Ward-Thompson & Barsony 1993).

Monte Carlo radiative transfer modelling by Choi et al. (1995) was successful in describing the observed line emission towards the centre of the molecular cloud in the context of the well-known spherically symmetric ‘inside out’

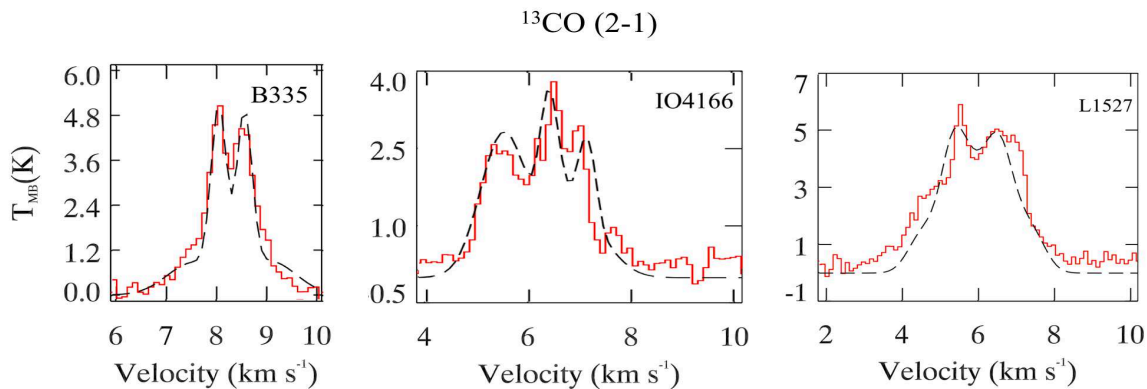


Figure 1. ^{13}CO ($J = 2 - 1$) line profiles at the (0,0) offset position for B335, IO4166 & L1527.

collapse model of Shu (1977). An infall (‘collapse expansion wave’) radius of 0.035 pc was deduced (Zhou et al. 1993). The expected density profile within the free-fall zone ($\propto r^{-1.5}$) is consistent with near-infrared extinction maps by Harvey et al. (2001). Outside the infall radius the density profile is consistent with that expected for a static singular isothermal sphere (Saito et al. 1999; Shirley et al. 2000).

Emission from a bipolar molecular outflow was observed in molecular line spectra by Moriarty-Schieven & Snell (1989). The outflow is very close to the plane of the sky ($\sim 10^\circ$) and is elongated in the east-west direction (Cabrit, Goldsmith & Snell 1988; Hirano et al. 1988; Saito et al. 1999).

2.2 IO4166

IO4166 is a protostellar object located in the Taurus molecular cloud at a distance of 140 pc (Elias 1978) and contains the IRAS source 04166 + 2706 (Kenyon et al. 1990). The radius of the molecular gas cloud has been estimated from the extent of molecular line emission from the high density tracers NH_3 (1,1) & (2,2) and from 1.2 mm continuum emission. Both are coincident out to a distance of 0.03 pc (Tafalla et al. 2004). Motte & André (2001) constructed a SED which is consistent with a Class 0 source and observations of N_2H^+ ($J = 1 - 0$) by Chen, Launhardt & Henning (2007) inferred a mean molecular hydrogen number density, $n_{\text{H}_2} = 4 \times 10^6 \text{ cm}^{-3}$.

IO4166 contains a highly collimated molecular outflow. The axis position angle (PA) is 30° (east of north) and extends 0.25 pc either side of the IRAS source (Bontemps et al. 1996). Tafalla et al. (2004) observed the outflow in ^{12}CO ($J = 2 - 1$) emission and found there are two distinct velocity components, one is at 50 km s^{-1} and a slower component with a velocity $< 10 \text{ km s}^{-1}$. A faster gas component is usually associated with the youngest of protostellar objects (Bachiller 1996). The slow gas is believed to be created by a shear flow of accelerated ambient gas moving along the wall of an evacuated cavity.

2.3 L1527

Like IO4166, L1527 is a protostellar core located in the Taurus molecular cloud at a distance of 140 pc and it contains the IRAS source 04368+2557 (Elias 1978). Double

peaked asymmetric line spectra consistent with gravitationally infalling gas was observed by Zhou et al. (1994) and Myers et al. (1995). Observations by Zhou, Evans & Wang (1996) and radiative transfer modelling by Myers et al. (1995) determined an infall radius of 0.03 pc. Continuum observations from $100 \rightarrow 800 \mu\text{m}$ shows the gas density profile varies as $r^{-1.5}$ within a radius of 0.03 pc. An upper limit to the age of this source was calculated by Ohashi et al. (1997) to be 10^5 yrs on the assumption of a constant accretion rate. However, Kenyon et al. (1993) found that a fit to the SED gives a lower age of 4.6×10^3 years indicating this is a young Class 0 source (André, Ward-Thompson & Barsony 1993).

A molecular outflow was observed in single dish and interferometric observations by MacLeod, Avery & Harris (1994) and Tamura et al. (1996). The outflow emission has an hourglass morphology (Zhou, Evans & Wang 1996; Ohashi et al. 1997) with the outflow axis at $< 10^\circ$ to the plane of the sky (Tamura et al. 1996).

More recent *Spitzer* observations of L1527 have clearly revealed the bipolar outflow structure but have also identified the presence of a ‘dark lane’ which has been ascribed to a modified inner envelope/outflow cavity morphology (Tobin et al. 2008). This inner ‘nozzle’ has a distinct effect on the *Spitzer* and near-infrared images of the source, but the scale of the structure ($\sim 100 \text{ au}$) is such that it would not significantly affect line profiles as observed at single-dish resolution.

3 OBSERVATIONS AND DATA

Line observations of our sources were made with the James Clerk Maxwell Telescope (JCMT) over a period of 18 months (mostly in service mode) using heterodyne receivers. We obtained a variety of strip and five-point maps for the various sources/transitions that we have considered, which have given sufficient data coverage of our sources so as to allow accurate modelling. We have also used JCMT-SCUBA (the Submillimeter Common-User Bolometer Array) archival data for $450/850 \mu\text{m}$ continuum emission.

3.1 Molecular Line Observations

The cores were observed with RxA3 (and RxA2) in August 2001 and March-May 2003. All observations were made in frequency switching mode and the details of the transitions

Table 1. The observed line emission tracers modelled in this paper.

Source	Molecule	Transition	$n_{\text{crit}} \text{ cm}^{-3}$	Receiver	Date Observed
B335	H ¹³ CO ⁺	($J = 3 - 2$)	3.4×10^6	A3	20 - August - 2001
	HCO ⁺	($J = 3 - 2$)	1.8×10^6	A2	18 - February - 1997
	¹³ CO	($J = 2 - 1$)	9.6×10^3	A3	15 - May - 2003
	C ¹⁸ O	($J = 2 - 1$)	9.5×10^3	A3	3 - May - 2003
	C ¹⁷ O	($J = 2 - 1$)	1.0×10^4	A3	3 - May - 2003
I04166	¹³ CO	($J = 2 - 1$)	9.6×10^3	A3	1 - April - 2003
	C ¹⁸ O	($J = 2 - 1$)	9.5×10^3	A3	18 - March - 2003
	C ¹⁷ O	($J = 2 - 1$)	1.0×10^4	A3	3 - May - 2003
L1527	H ¹³ CO ⁺	($J = 3 - 2$)	3.4×10^6	A3	3 - May - 2003
	¹² CO	($J = 2 - 1$)	1.1×10^4	A3	3 - May - 2003
	¹³ CO	($J = 2 - 1$)	9.6×10^3	A3	3 - May - 2003
	C ¹⁸ O	($J = 2 - 1$)	9.5×10^3	A3	3 - May - 2003
	C ¹⁷ O	($J = 2 - 1$)	1.0×10^4	A3	3 - May - 2003

Table 2. Flux Calibration Factors from photometry observations of Uranus. The calibration factors listed are determined for 40'' and 120'' beams. Emission maps at 450 μm and 850 μm of B335, L1527 and 04166 were originally published in Shirley et al. (2000).

Source	α (J2000)	δ (J2000)	τ_{850} (Jy V ⁻¹)	τ_{450} (Jy V ⁻¹)	Date (Jy V ⁻¹)	FCF ₄₀ ⁸⁵⁰ (Jy V ⁻¹)	FCF ₁₂₀ ⁸⁵⁰	FCF ₄₀ ⁴⁵⁰	FCF ₁₂₀ ⁴⁵⁰
B335	19 37 01.13	07 34 10.9	0.14	0.69	17-April-1998	1.01	0.86	5.84	3.98
I04166	04 19 42.5	27 13 36	0.17	0.77	30-August-1998	0.98	0.77	5.32	3.74
L1527	04 39 53.89	26 03 10.5	0.15	0.76	24-January-1998	1.02	0.92	5.76	5.34

are given in Table 1. The data were reduced using the SPECX software package and further analysis was undertaken with the CLASS package of IRAM. For the majority of the observations, the system temperature was between 300 and 450 K. A main beam correction factor of 0.69 was used to convert the antenna temperatures into T_{MB} . The critical density for thermalisation (n_{crit}) for each transition is also given in Table 1. These show the wide range of densities ($9 \times 10^3 - 3 \times 10^6 \text{ cm}^{-3}$) that are probed by the chosen molecular tracers/transitions.

3.2 Dust Continuum Observations

Archival SCUBA data of our three sources was retrieved and reduced using the SURF package. The data consists of dust continuum emission observed at 850 μm and 450 μm . All our science observations are 64-point jiggle maps with a 120'' chop throw. Wavelength dependent submillimeter extinction, τ_{850} and τ_{450} were calculated from skydip observations. Bolometers at the edge of the array and those with excessive noise ($V_{\text{rms}} \geq 60 \text{ nV}$) were removed before the data was rebinned to 0.5 θ_{MB} per pixel on a J2000 coordinate system. The SCUBA emission maps were converted to Jansky units using FCFs calculated from photometry observations of Uranus. The FCFs for each source are listed in Table 2 for each source.

4 MODELLING

4.1 The Physical Model

For the purpose of the radiative transfer modelling we have used a simple dynamical model that is similar to that described in Rawlings et al. (2004). This is a multi-component physical construct that includes a static envelope of molecular gas whose density varies with radius from the centre of the gas cloud and a bipolar outflow. The temperatures in the envelope and the outflow interface components are taken to be spatially invariant. This is obviously a significant simplification but, as shown in Tsamis et al. (2002), in the case of the low-J lines observed at low spatial resolution that we are modelling, the line profiles are generally more sensitive to abundance variations and the gas dynamics than they are to the temperature profile. Obviously, this assumption breaks down in the case of smaller beams and/or higher levels of excitation. It is assumed that the envelope and the outflow are dynamically decoupled from each other as the interactions between the two are most likely limited to narrow interface regions.

The envelope comprises the quasi-static gas reservoir that surrounds a protostellar core and, initially, has a density structure that is described by the Lane - Emden equation (Chandrasekhar 1967). Bonner - Ebert (BE) spheres provide a set of solutions for isolated, pressure-bound, spherically symmetric isothermal clouds in hydrostatic equilibrium and of varying density contrast between the centre and the edge of the cloud (Bonner 1956; Ebert 1955). The sources that we are studying

have evolved beyond the initial stage of hydrostatic equilibrium and early collapse and we approximate the gas distribution with the simple Plummer density profile (Arreaga-García, Klapp-Escribano & Gómez-Ramírez 2010)

$$\rho(r) = \frac{\rho_0 R_0^2}{(R_0^2 + r^2)} \quad (1)$$

where ρ_0 is the peak gas density and R_0 is the radius within which the density is ρ_0 . This profile is similar to the Bonnor - Ebert solution, retaining the $1/r^2$ shape at large radii, but has a somewhat flatter density distribution in the more central regions, as applicable to more evolved objects. The adoption of other representations of the density structure, such as simple power laws, or the Bonnor - Ebert solution, actually has very little effect on the results. This is because the differences between the profiles are greatest in the central regions which are poorly resolved and beam-diluted.

The outflow is driven by a high speed, low density hot jet which, through turbulent shear, accelerates the molecular gas. Within the outflow the temperature, velocity and density will vary with distance from the jet axis. Observations (e.g. Gueth & Guilloteau 1999) indicate that the highest velocity and most excited molecular gas is typically located in a narrow region close to the underlying jet. For convenience the molecular outflow is divided into two regions, a hot, low density inner region which is close to the protostellar jet (hereafter the ‘inner boundary layer’) and a denser, cooler region at the interface between the outflow envelope (hereafter the ‘outer boundary layer’). A better approximation would be a linear variation in the outflow parameters between the interface with the jet and with the envelope; however, due to the resolution of the single dish observations being modelled, this refinement would result in little change to the line profiles. So, for simplicity, we employ a two-component molecular outflow model.

Following Rawlings et al. (2004) and Carolan et al. (2008, 2009) the shape of the molecular outflow is constructed using a \tanh function to approximate to the observed morphology of the base of the outflowing molecular gas. The equation defining the edge of the outer boundary layer is,

$$z = \tanh(\lambda r), \quad (2)$$

where z and r are the ordinates along and perpendicular to the outflow axis respectively. Thus, λ defines the shape of the flow. A value of $\lambda = 2$ gives a morphology consistent with typical interferometric observations of low velocity outflows (e.g. Lee et al. 2002; Arce & Goodman 2002; Jørgensen et al. 2007). The edge between the inner and outer boundary layers is defined by a value of $\lambda = 2.2$ (as in Rawlings et al. 2004; Carolan et al. 2008) so that $\sim 10 - 20$ percent of the outflow is contained within the outer boundary layer. Within this layer, the velocity of the gas was maintained at a constant speed with a direction tangential to the inside edge of the boundary layer. Within the inner boundary layer, the velocity of the gas was maintained at a constant radial velocity. For the sake of simplicity, in this model the density is taken to be constant within each of the boundary layers. More complex geometries (including density and velocity gradients) were found not to have significant impacts on the line profiles. Figure 2 is an example schematic

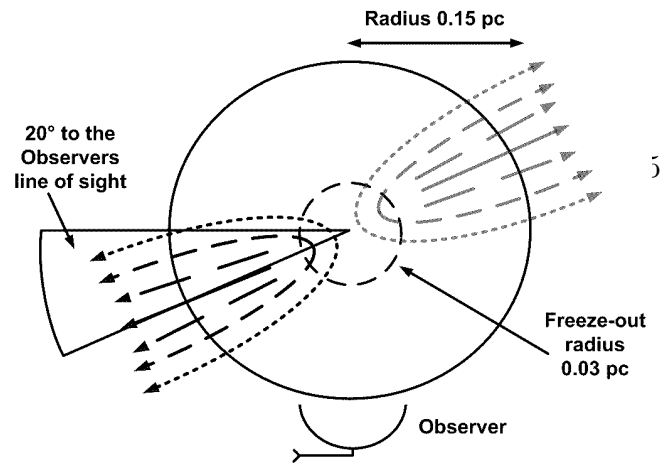


Figure 2. Schematic diagram of the dynamical model. The dashed line is the outer boundary layer, the broken lines are the inner boundary layer and the solid line represents the unobserved underlying jet. The viewing angle (the tilt between the axis of the outflow lobes and the plane of the sky) and freeze-out radius are for I04166. The dynamical models for L1527 and B335 have different viewing angles and radii, recorded in Table 3.

diagram of the model used for I04166. Whilst this model is simplistic, it is consistent with the observational effects that can be detected at single-dish resolution. Real outflow sources will have more complex (sub-)structure (e.g. as seen in L1527 - Tobin et al. 2008) but on scales that will not significantly affect the line profiles as observed at $\sim 10 - 20''$ resolution.

4.2 Radiative Transfer Modelling

In order to interpret the observed line emission profiles, a thorough analysis of the spectra must account for the simultaneous processes of infall, outflow, gas freeze-out and desorption including the contributions to the profile formation at all points along the line of sight.

We have utilised a 3D radiative transfer code, MOLLIE (MOlecular LIne Explorer)¹, written and developed by Keto and collaborators (see, e.g. Keto 1990; Keto et al. 2004; Redman et al. 2004; Redman, Keto & Rawlings 2006; Carolan et al. 2008, 2009; Longmore et al. 2011, for examples of its use). MOLLIE is used to generate synthetic line profiles to compare with observed rotational transition lines. In order to calculate the level populations the statistical equilibrium equations are solved using an Accelerated Lambda Iteration (ALI) algorithm (Rybicki & Hummer 1991) that reduces the radiative transfer equations to a series of linear problems that are solved quickly even in optically thick conditions. MOLLIE splits the overall structure of a cloud into a 3D grid of distinct cells.

The input to MOLLIE is divided into voxels (3D pixels) and there are five input parameters which need to be uniquely defined for each voxel: the number density of H_2 ; the gas temperature; the gas bulk velocity; the microturbulent velocity of the gas; and the chemical abundance. As described in the next section, the parameters other than the abundance can each be constrained from the continuum and molecular observations, coupled with radiative transfer calculations.

Carolan (2009) calculated the chemical abundances in a detailed chemical model for simple spherically symmetric clouds and investigated the sensitivity of the resulting molecular line profiles to the chemical variations. He found

¹ <https://www.cfa.harvard.edu/eketo/mollie/documentation>

that, because the largest chemical changes tend to take place in the centre of the cloud (as a result of molecular freeze-out), the CO abundance in the bulk of the volume of the cloud can be taken to be approximately constant. Again, we note that the line profiles convolved to the resolution of single dish observations do not significantly resolve the chemical variations. Therefore, we have not performed any chemical modelling in this study, rather we use the observations to constrain the molecular abundance for each of the envelope, inner boundary layer and outer boundary layer in the sources.

Subsequently we perform a chi-squared analysis to find the best fit parameters. This procedure works by running a series of simulations with the abundance kept constant whilst the other four parameters are varied. This is repeated for different abundances until a best fit is found (Carolan 2009).

5 ANALYSIS AND RESULTS

The chi-squared analysis described above can be used to obtain best fit parameters from an arbitrary first approximation but, wherever feasible, we try to simplify the procedure by using simple analyses of observational data to constrain as many of the free parameters as possible. These values are then refined by the modelling/chi-squared fitting analysis.

In practice, this is not possible for the outflow and interface components. However, in the case of the envelope, if we make the assumptions described above (spherical symmetry, density structure described by a Plummer law, and isothermality) we can make some rough first estimates of the key physical parameters, using optically thin $C^{18}O$ ($J = 2 - 1$) line and/or dust continuum emission data.

Using this approach we obtain constraints on the following quantities: (a) the characteristic radius within which the CO abundance is significantly reduced as a result of freeze-out onto dust grains, by (b) a representative depletion factor, (c) the normalisation (ρ_0, R_0) for the (Plummer) density profile, (d) the gas temperature, and (e) the turbulent velocity. The (highly simplified) procedure that we adopt is as follows:

CO freezes out onto the surface of dust grains at low temperatures ($T \lesssim 20\text{K}$) and high densities ($n_{H_2} \gtrsim 10^4 \text{ cm}^{-3}$) (Sandford & Allamandola 1993). To determine the degree of freeze-out we compare spatial distributions of the H_2 column density as determined from the dust continuum observations to those determined from molecular (CO) observations. The offset between the two gives a measure of the amount of molecular depletion on the assumption that freeze-out is the the only cause of the CO abundance reduction. The absolute normalisation will depend on such factors as the dust opacity, the dust-to-gas ratio and the (assumed constant) CO: H_2 ratio, and so is highly uncertain, but the relative variations across the core will be reasonably well-defined.

The column density of H_2 can be derived from the dust continuum fluxes using the equation

$$N_{H_2} = \frac{S_{850}}{\Omega \kappa_{850} \mu m_H B(T_{\text{dust}})}, \quad (3)$$

where m_H is the mass of a hydrogen atom and μ is the mean

molecular weight. S_{850} is the flux in Jy at $850\mu\text{m}$, Ω is the aperture solid angle in steradians; $\Omega = (\pi\Theta^2)/(4 \ln 2)$, where Θ is the beam size in radians. We have measured the flux in a $21''$ beam so that a suitable comparison to the $C^{18}O$ $J = 2 - 1$ observations (made with a HPBW of $21''$) can be made. The Planck function $B(T_{\text{dust}})$ is calculated assuming a uniform dust temperature of 10K . This is a simplification, but a number of other studies (e.g. Evans et al. 2005) have shown a beam-averaged temperature of $\sim 10\text{K}$ is appropriate for Class 0 sources. There will obviously be some deviations from this value near the outer edge of the envelope, and close to the protostar but, at single dish resolution we find that the effects are marginal. A dust mass opacity of $\kappa_{850} = 0.02 \text{ cm}^2 \text{ g}^{-1}$ is assumed which is consistent with Ossenkopf & Henning (1994) - being representative of dust grains with thin ice mantles. The dust to gas ratio is taken to be 100.

The column density of H_2 has also been determined from molecular gas observations using the optically thin rotational transition $C^{18}O$ ($J = 2 - 1$), with the simplifying assumptions of isothermality and a standard CO: H_2 ratio. This analysis is fully described in Appendix A.

Figure 3 shows comparisons between the two as observed in each of the three sources. The dust emission profiles closely match the results from previous studies (e.g. Shirley, Evans, & Rawlings 2002). Each plot in Figure 3 clearly shows the presence of depletion, which becomes more significant as one approaches the centre of each core. We simplify the complexity of this structure by a step function, so that a nominal depletion radius is defined for each source, within which the gas-phase CO abundance is reduced by a factor of between 3 and 10. These parameters are initially estimated from Figure 3 and then further refined by the modelling/fitting technique.

Using a Plummer law for the density profile and assuming spherical symmetry in the envelope we then use the column densities of H_2 derived from the (undepleted) dust continuum emission to determine the normalisation factors (R_0, ρ_0) in equation 1 and hence the number density of H_2 : n_{H_2} .

The dust temperature was found by first re-binning the $450\mu\text{m}$ emission to $14''$ which is the size of the beam at $850\mu\text{m}$. A flux density is then extracted which is the azimuthal average of the flux density in a $14''$ aperture. The flux density was measured at $7''$ spacing to ensure that the emission is Nyquist sampled. Note that this assumes a perfect (gaussian) beam. In practice, we find that the inclusion of the error beams at 450 and $850\mu\text{m}$ makes very little difference to this analysis. The temperature can then be estimated from the ratio of the fluxes at 450 and $850\mu\text{m}$. At these wavelengths there are significant departures from the Rayleigh-Jeans approximation and the flux ratio is given by;

$$\frac{S_{450}}{S_{850}} = \left(\frac{850}{450}\right)^{3+\beta} \frac{\exp(17\text{K}/T_{\text{dust}}) - 1}{\exp(32\text{K}/T_{\text{dust}}) - 1} \quad (4)$$

(Kramer et al. 2003), where S is the flux in a $14''$ beam, T_{dust} is the dust temperature and β is the dust emissivity index. For the purposes of our analysis we use $\beta = 1.5$ which is characteristic of dust grains in cold molecular clouds, is reasonably consistent with Ossenkopf & Henning (1994) and is within the limits of variation ($1 \leq \beta \leq 2$) expected for molecular clouds (Schnee & Goodman 2005).

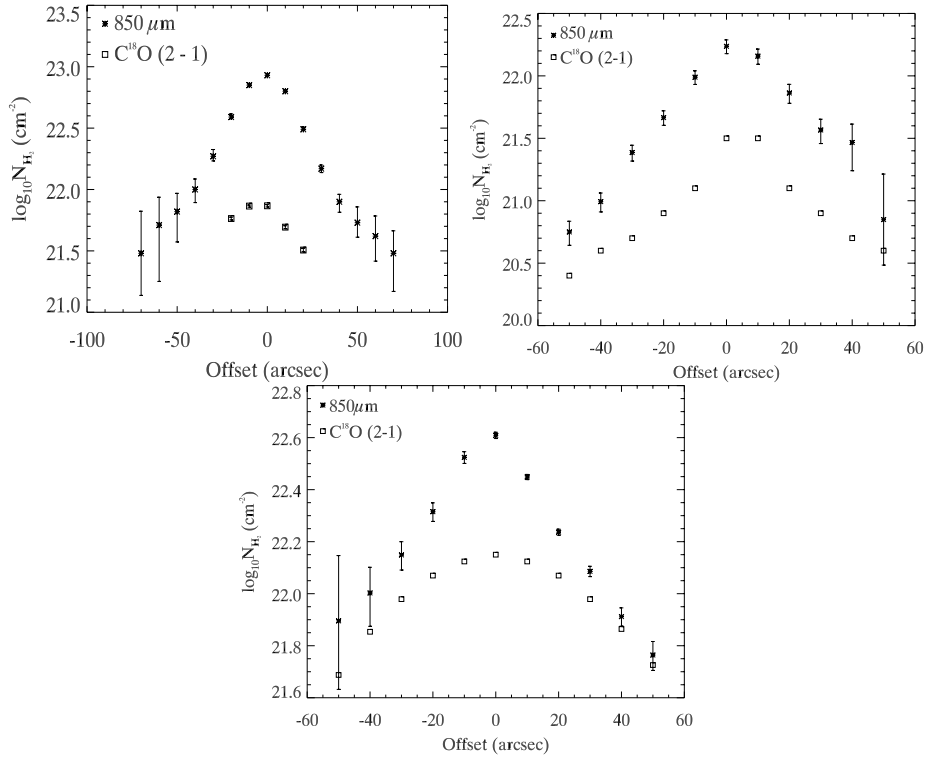


Figure 3. A comparison of the column density of H_2 derived from SCUBA dust continuum and integrated $C^{18}O$ molecular line emission for B335, I04166 and L1527 respectively.

There are a couple of major assumptions with this method; (i) We assume that the dust and gas are well-coupled, in which case a single value can be used to describe both the gas and the dust temperatures. For the dense cores that we are investigating this is a fair approximation. (ii) We do not allow for any spatial variation in temperature across the envelope. This is known not to be the case (e.g. Shirley, Evans, & Rawlings 2002) but the magnitude of those variations are not sufficient to warrant a more detailed approach in a simple model that is tailored to what can be detected at single-dish resolution.

Finally, the turbulent velocity, σ_{NT} , is estimated on the assumption that turbulence is the sole non-thermal component of the line broadening for the (optically thin) single peaked $C^{18}O$ ($J = 2 - 1$) lines. In which case;

$$\sigma_{tot}^2 = \sigma_{NT}^2 + \sigma_T^2, \quad (5)$$

where σ_{tot} is the total velocity dispersion and is related to the observed FWHM of a representative molecular line profile (Δv) by $\sigma_{tot}^2 = \Delta v / \sqrt{8 \ln 2}$. σ_T is the thermal velocity dispersion given by $\sigma_T^2 = kT/\mu$, where μ is the molecular mass, T is the gas temperature and k is Boltzmann's constant.

5.1 Radiative Transfer Modelling of the Observed Spectral Line Emission

Our results and best-fit parameters are described in this section for each of our three sources. Table 1 lists the molecular transition observed for each source and the results are presented in figures 4-16 with the observed emission line profiles overlaid with the best fit modelled profiles. The best

fit model parameters are given in tables 3-5. The number of significant figures given in these tables indicates the level of accuracy obtained by the chi-squared fitting technique.

5.1.1 B335

B335 was observed in several molecular species/transitions. Line profiles of the optically thin ($J = 2 - 1$) transition of $C^{17}O$ and $C^{18}O$ are shown in Figures 4 & 5. They are shown as a strip of spectral line profiles that are centered at the peak of $850\mu m$ dust continuum emission which corresponds to the (0,0) offset in both Figures 4 and 5.

The observed line emission profile of $C^{17}O$ ($J = 2 - 1$) arises from separate hyperfine line transitions whose peaks are clearly distinguishable in Figure 4. In a highly turbulent gas the components would be blended. The spectra of $C^{18}O$ ($J = 2 - 1$) are single peaked and have similar intrinsic line widths as the $C^{17}O$ ($J = 2 - 1$) lines. It would therefore seem that both transitions are preferentially probing cold, quiescent gas in the envelope. The best fit parameters from the radiative transfer modelling of the molecular gas envelope are listed in Table 3. Blanks in the table imply that the line profiles are insensitive to the abundances which are therefore unconstrained by the model.

The turbulent velocity in the envelope gas was calculated to be 0.25 km s^{-1} as determined from the $C^{18}O$ ($J = 2 - 1$) line profiles. To account for the observed molecular depletion, as evident in Figure 3, the $C^{18}O$ ($J = 2 - 1$) and $C^{17}O$ ($J = 2 - 1$) line profiles were modelled with an abundance that is reduced by a factor of ten inside a freeze-out radius of $\sim 0.3 \times$ the core radius.

The best fit abundances of $C^{18}O$ obtained inside and

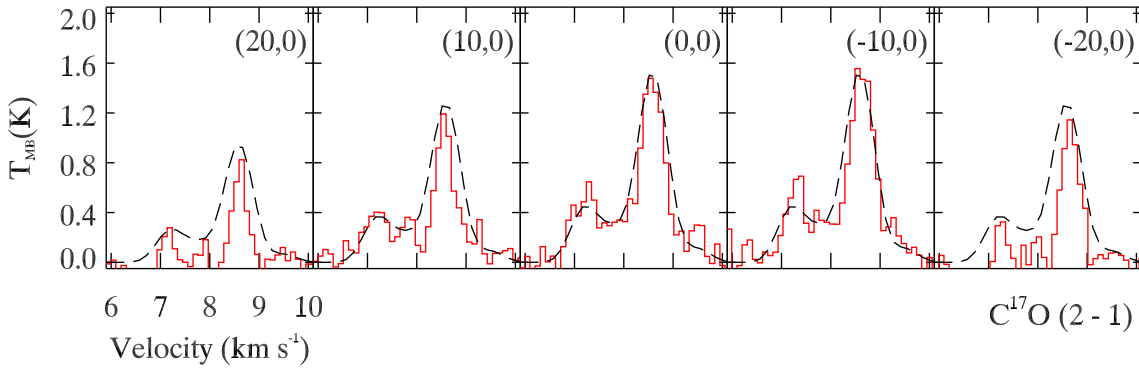


Figure 4. B335: C^{17}O ($J = 2 - 1$) line profiles: observed (solid line) and modelled (dashed line). The offset between cells is $10''$.

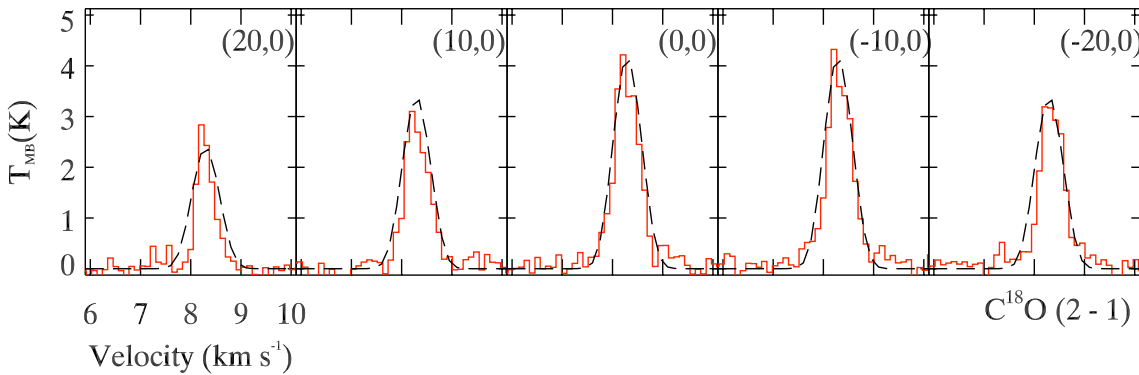


Figure 5. B335: C^{18}O ($J = 2 - 1$) line profiles: observed (solid line) and modelled (dashed line). The offset between cells is $10''$.

outside the freeze-out region are 3×10^{-8} and 3×10^{-7} respectively. These are similar values to those obtained by Evans et al. (2005): $2.5 \times 10^{-8}/7.4 \times 10^{-8}$. C^{17}O was modelled with the same depletion factor so that the best fit abundances were $0.35 \times 10^{-8}/3.5 \times 10^{-8}$. This implies a value for the $^{18}\text{O}:^{17}\text{O}$ ratio that is a factor of $\sim 2 \times$ larger than interstellar values (Schöier et al. 2002).

Figure 6 shows the observed line spectra and the modelled profiles for HCO^+ ($J = 3 - 2$). The observational data consists of a single line profile at zero offset. H^{13}CO^+ ($J = 3 - 2$) line profiles are shown in Figure 7. Although clearly present in the zero offset position, there is barely any emission detected in the ($20''$) off centre spectra. This is not surprising as the critical densities of the transitions are $1.8 \times 10^6 \text{ cm}^{-3}$ and $3.4 \times 10^6 \text{ cm}^{-3}$ respectively; larger than the peak H_2 density in B335.

The values of the temperature, peak density, infall and turbulent velocities were constrained from the C^{18}O ($J = 2 - 1$) & C^{17}O ($J = 2 - 1$) lines. The best fit HCO^+ abundance is 3×10^{-8} which agrees well with the value (3.5×10^{-8}) obtained by Evans et al. (2005). The H^{13}CO^+ best fit abundance is 9×10^{-10} . The ratio $\text{H}^{12}\text{CO}^+/\text{H}^{13}\text{CO}^+$ is ≈ 39 . This is less than the standard interstellar abundance ratio $^{12}\text{C}/^{13}\text{C} \sim 70$ measured in atomic clouds (Wilson & Rood 1994) and may be indicative of chemical fractionation effects as discussed below.

Figure 8 shows the observed and modelled line emission spectrum for ^{13}CO ($J = 2 - 1$). The line profiles are double peaked and asymmetric. The critical density for this transition is three orders of magnitude less than the peak

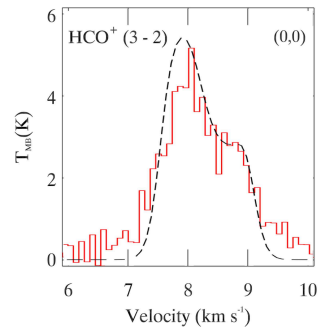


Figure 6. B335: HCO^+ ($J = 3 - 2$) line profiles: observed (solid line) and modelled (dashed line). The middle panel is at $0''$ offset.

density in B335 so that it probes the optically thick gas far from the centre of the cloud. The asymmetry changes from red-asymmetric (i.e. red>blue) at ($20,0$) to blue-asymmetric at ($-20,0$).

Asymmetric, double peaked line profiles are often taken to be signatures of the presence of infall. However, such an explanation fails to explain the facts that (a) both red and blue-asymmetry are present, and (b) asymmetric emission is present at significantly greater offsets ($> 10''$) than expected for an infall source. A bipolar outflow is therefore a much more likely cause and naturally gives rise to spatially distinct redshifted and blueshifted components. Moreover, outflowing gas has been observed in ^{12}CO ($J = 2 - 1$) by Moriarty-Schieven & Snell (1989) extending to 0.36 pc ($5'$) either side of IRAS 19347+0727. The emission is observed

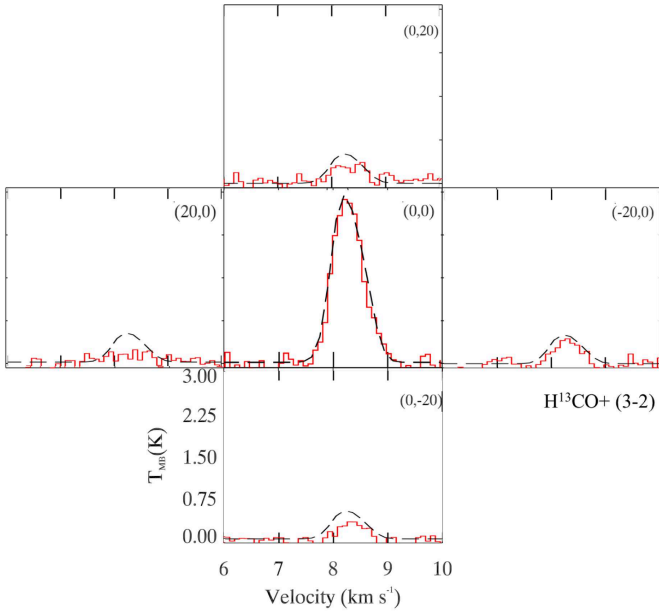


Figure 7. B335: H^{13}CO^+ ($J = 3 - 2$) line profiles: observed (solid line) and modelled (dashed line). The offset between cells is $20''$ and the middle panel is at $0''$ offset.

to increase in intensity at the lobe edge. The asymmetry in the line emission profile is essentially caused by the axis of outflow axis being tilted to the line of sight. Tables 4 & 5 specify the the best fit parameters for the gas in the outer and inner boundary layer of the outflow.

5.1.2 I04166

Observations of C^{17}O and C^{18}O ($J = 2 - 1$) towards I04166 are shown in Figures 9 and 10. The line profiles shown in Figure 9 clearly show the C^{17}O ($J = 2 - 1$) hyperfine line transitions whilst the C^{18}O ($J = 2 - 1$) lines shown in Figure 10 are single-peaked and narrow. Both are characteristic of the quasi-static/slowly infalling gas in the molecular gas envelope. Best fit parameters for these profiles (applying to the molecular envelope) are given in Table 3. There is little contribution to the modelled line profile from gas residing in the molecular outflow. We also note that the peak density, as obtained from the $850\mu\text{m}$ continuum observations is consistent with previous estimates derived from N_2H^+ ($J = 1 - 0$) observations (Chen, Launhardt & Henning 2007).

The line profiles for ^{13}CO ($J = 2 - 1$) are shown in Figure 11. This shows the standard blue-asymmetric double-peaked line profile suggestive of infalling gas. In addition there is a component at 5.5 km s^{-1} which is also seen in the optically thin C^{18}O ($J = 2 - 1$) and, to a lesser extent, C^{17}O ($J = 2 - 1$) line profiles. It has also been detected in the line profiles of CS ($J = 2 - 1$) and H_2CO ($2_{12} - 1_{11}$) (Mardones et al. 1997).

The best fit parameters for the infalling envelope component are given in Table 3. The high velocity gas component at 5.5 km s^{-1} can be explained by emission originating from the outer boundary layer with the parameters given in Table 4. The wings of the line profile are explained by the high velocity warm gas in the inner boundary layer that is close to the protostellar jet. The best fit parameters for this

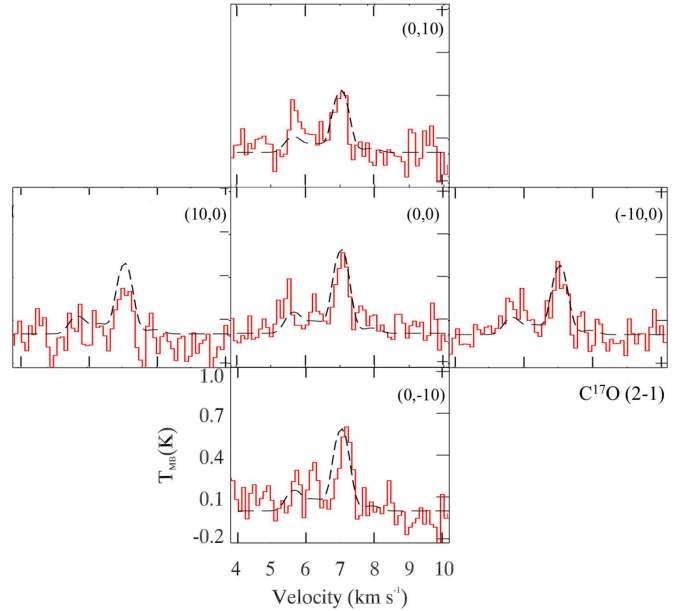


Figure 9. I04166: C^{17}O line profiles: observed (solid line) and modelled (dashed line). The offset between cells is $10''$.

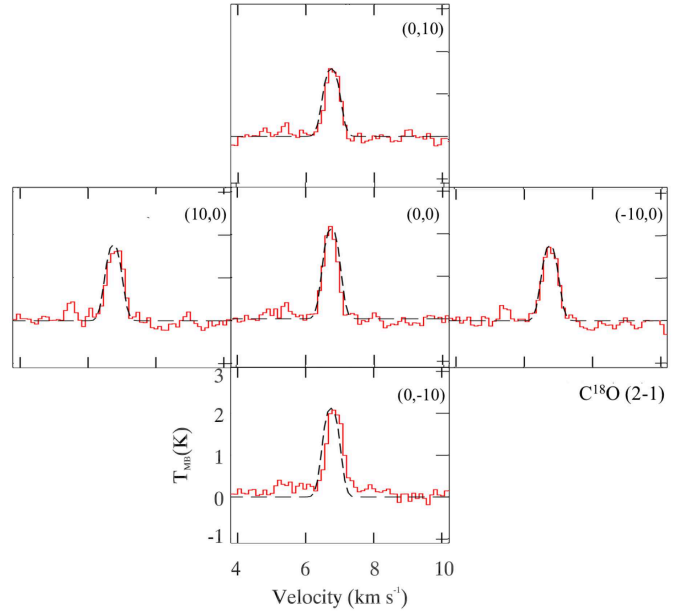


Figure 10. I04166: C^{18}O line profiles: observed (solid line) and modelled (dashed line). The offset between cells is $10''$.

gas are given in Table 5. Note that the blueshifted emission seen in Figure 11 is dominant due to the greater amount of absorbing gas on the redshifted side (Tafalla et al. 2004; Santiago-Garcia et al. 2009).

5.1.3 L1527

Figures 12 and 13 show the modelled and observed C^{17}O and C^{18}O ($J = 2 - 1$) line profiles respectively, whilst Figure 14 shows the H^{13}CO^+ ($J = 2 - 1$) line. All three profiles are successfully modelled as originating from the molecular gas in the envelope. Specifically, there is no contribution to these

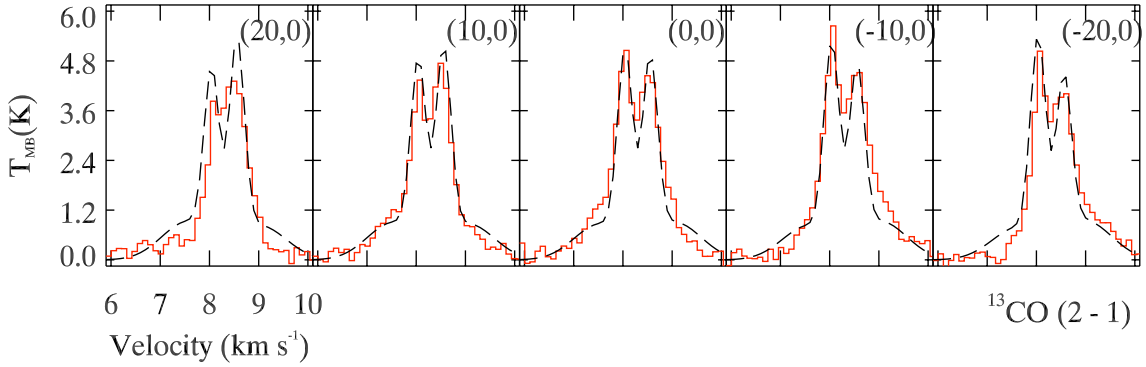


Figure 8. B335: ^{13}CO ($J = 2 - 1$) line profiles: observed (solid line) and modelled (dashed line). The offset between cells is $10''$.

Table 3. Best fit parameters for the gas in the envelope of each source. The first eight parameters were roughly constrained by observations and then fine tuned to improve the model fits. The outflow tilt angle is relative to the plane of the sky and the abundance is the column density ratio relative H_2 .

Envelope Parameters	B335	I04166	L1527
Outflow tilt angle (degrees)	-10	20	10
Source radius (pc)	0.15 pc	0.15 pc	0.08 pc
Depletion radius (pc)	0.05	0.03	0.015
CO depletion factor	10	3	3
Temperature (K)	20	20	20
Peak Density (cm^{-3})	10^6	4×10^6	10^6
Velocity (km s^{-1})	-0.3	-0.2	-0.3
Turbulent width (km s^{-1})	0.25	0.2	0.3
Abundance C^{17}O ($\times 10^{-8}$)	3.5	0.98	0.075
Abundance C^{18}O ($\times 10^{-8}$)	30	2.6	0.30
Abundance ^{13}CO ($\times 10^{-8}$)	180	6	5
Abundance ^{12}CO ($\times 10^{-8}$)			400
Abundance HCO^+ ($\times 10^{-8}$)	3		
Abundance H^{13}CO^+ ($\times 10^{-8}$)	0.09		0.0022

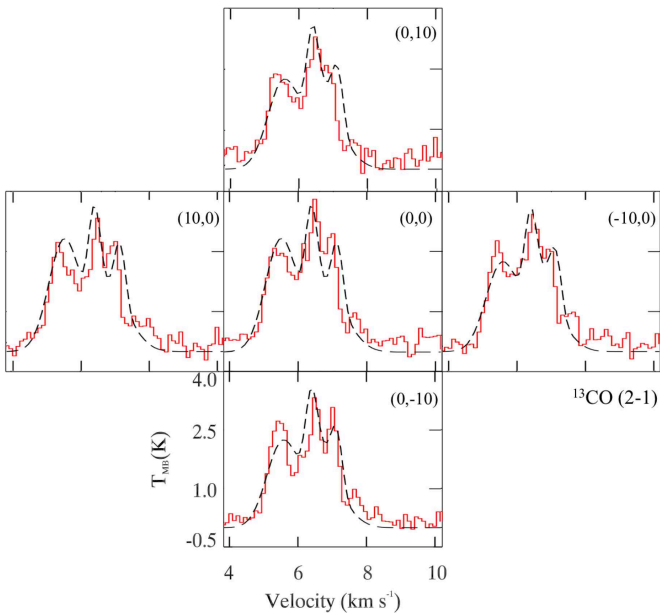


Figure 11. I04166: ^{13}CO ($J = 2 - 1$) line profiles: observed (solid line) and modelled (dashed line). The offset between cells is $10''$.

line profiles from the gas in the molecular outflows. The best fit parameters for these three lines are given in Table 3.

Figure 15 shows the modelled and observed line profiles of ^{13}CO ($J = 2 - 1$). The core of the line is well fit by emission from the envelope gas. However this fails to account for the emission in the wings of the line profile. The best fit parameters for the molecular gas in the outflow regions are listed in Table 4 and 5. The boundary layers of the molecular outflow are fit with a $^{13}\text{CO}:^{12}\text{CO}$ abundance ratio that is significantly enhanced relative to the gas in the envelope.

Figure 16 shows the ^{12}CO ($J = 2 - 1$) line emission. This transition traces the large-scale molecular outflow, extending $40''$ either side of the IRAS source which is located at the zero offset position. The line profiles are double peaked and asymmetric with the asymmetry changing from blue to red-asymmetric going from left to right in Figure 16. Again, this is indicative of the presence of a bipolar outflow. It is consistent with the findings of Myers et al. (1995) who deduced the presence of an outflow with a density $> 10^5 \text{ cm}^{-3}$ from observations of H_2CO ($2_{12} - 1_{11}$) & ($3_{12} - 2_{11}$).

6 DISCUSSION

In this section the results are discussed in terms of the molecular gas parameters of each of the three components in our

Table 4. Best fit parameters for the gas in the outer boundary layer. This corresponds to the molecular gas at the interface between the molecular outflow and the envelope. The first four parameters were constrained by observations and then fine tuned to improve the model fits. The abundances are relative to H₂.

Parameters Outer Boundary Layer		B335	I04166	L1527
Temperature	(K)	35	50	30
Peak Density	(cm ⁻³)	10 ⁵	10 ⁵	9 × 10 ⁴
Velocity	(km s ⁻¹)	1.4	1.2	1.3
Turbulent width	(km s ⁻¹)	0.3	0.4	0.4
Abundance ¹³ CO	(×10 ⁻⁸)	300	10	60
Abundance ¹² CO	(×10 ⁻⁸)			450
Abundance HCO ⁺	(×10 ⁻⁸)	9		

Table 5. Best fit parameters for the gas in the inner boundary layer of each source. The inner boundary layer is the molecular gas in the outflow that is closest to the protostellar jet. The first four parameters were constrained by observations and fine tuned to improve the model fits. The abundances are relative to H₂.

Parameters Inner Boundary Layer		B335	I04166	L1527
Temperature	(K)	55	80	60
Peak Density	(cm ⁻³)	10 ⁴	5 × 10 ⁴	10 ⁴
Velocity	(km s ⁻¹)	3.5	1.6	2.5
Turbulent width	(km s ⁻¹)	0.5	0.6	0.6
Abundance ¹³ CO	(×10 ⁻⁸)	600	12	400
Abundance ¹² CO	(×10 ⁻⁸)			600
Abundance HCO ⁺	(×10 ⁻⁸)	12		

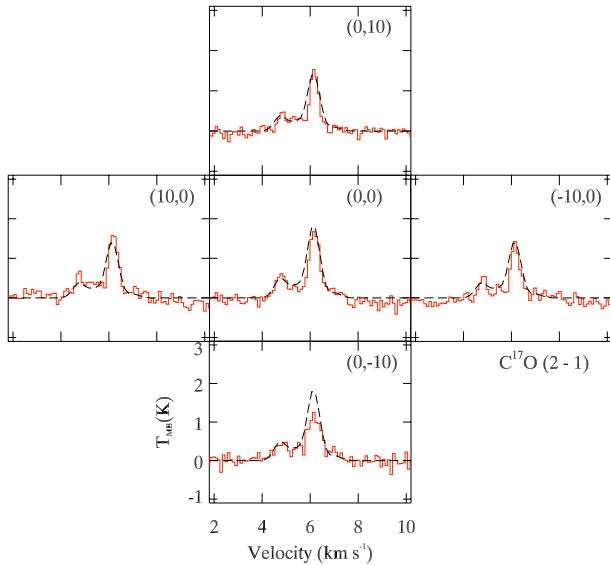


Figure 12. L1527: C¹⁷O ($J = 2 - 1$) line profiles: observed (solid line) and modelled (dashed line). The offset between cells is 10^{''}.

model; the molecular gas envelope surrounding the protostellar core and the inner and outer boundary layer regions of the molecular outflow.

6.1 Molecular Envelope

The abundances of C¹⁸O and C¹⁷O are well-constrained because the emissions originate from optically thin, quiescent,

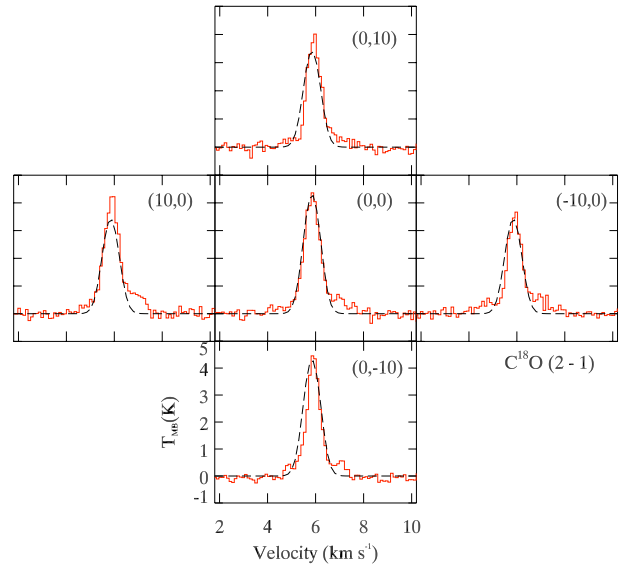


Figure 13. L1527: C¹⁸O ($J = 2 - 1$) line profiles: observed (solid line) and modelled (dashed line). The offset between cells is 10^{''}.

gas. The situation is somewhat complicated by the action of freeze-out which results in molecular depletion in the inner, denser parts of the core. This process is reversed at the smallest radii, due to heating by the protostar, but on a scale that would be undetectable at JCMT resolution. As described above, we have quantified the level of depletion by comparison of dust continuum and CO line emission maps and find that the maximum depletion factor is ~10 B335

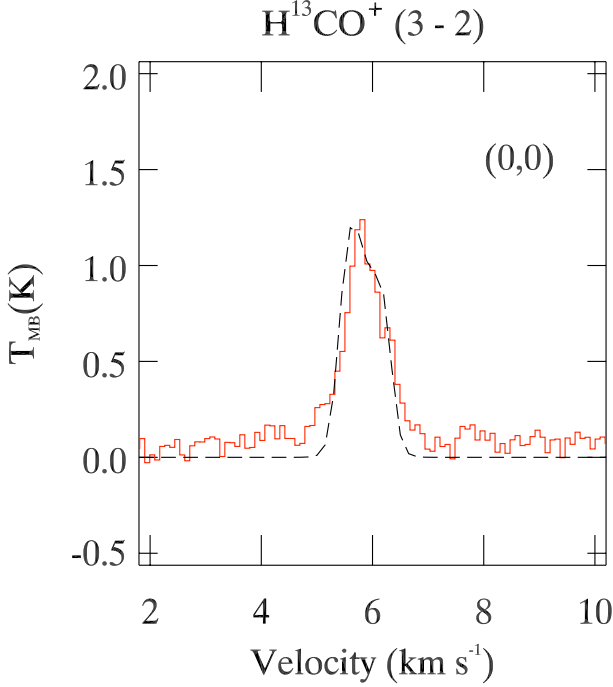


Figure 14. L1527: H^{13}CO^+ ($J = 2 - 1$) line profiles: observed (solid line) and modelled (dashed line). The offset between cells is $10''$.

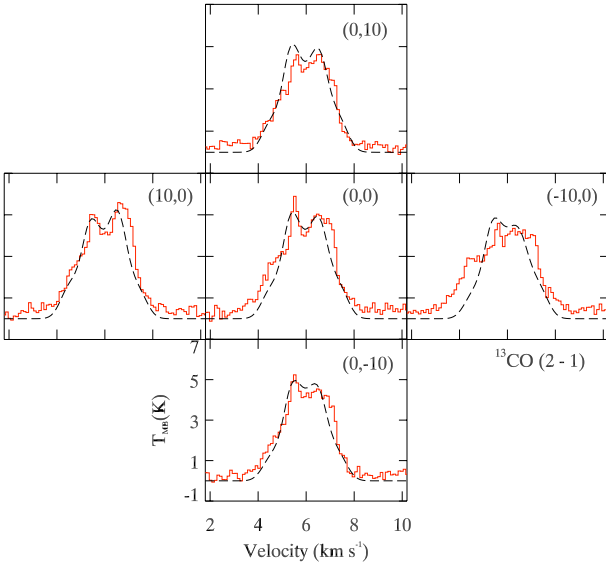


Figure 15. L1527: ^{13}CO ($J = 2 - 1$) line profiles: observed (solid line) and modelled (dashed line). The offset between cells is $10''$.

whilst for I04166 and L1527 it is ~ 5 . As B335 is the densest and has the largest dust column density of our three sources (see Figure 3) it is not surprising that it suffers the highest level of gas-phase depletion.

6.2 Outflow abundances in inner and outer boundary layer

The physical parameters of molecular gas in the outflow were constrained by modelling the observed line emission of ^{12}CO

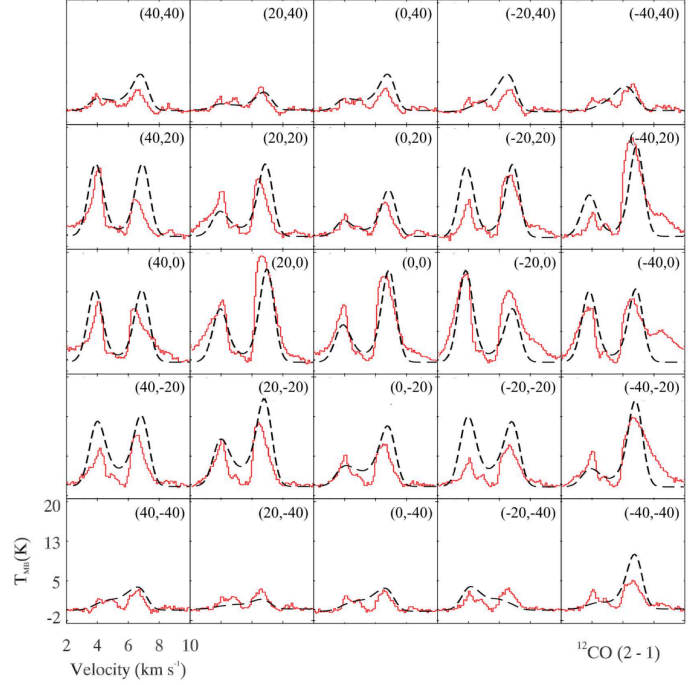


Figure 16. L1527: ^{12}CO ($J = 2 - 1$) line profiles: observed (solid line) and modelled (dashed line). The offset between cells is $10''$.

($J = 2 - 1$), ^{13}CO ($J = 2 - 1$) and HCO^+ ($J = 3 - 2$) towards each of the sources. Having large abundances, ^{13}CO ($J = 2 - 1$) and ^{12}CO ($J = 2 - 1$) transitions can be used to trace the full extent of the outflow. Although HCO^+ is abundant in our sources, the ($J = 3 - 2$) transition has a very high critical density so that it effectively only traces gas deep inside the molecular envelope close to the base of the outflow.

Table 4 and Table 5 show that the molecular abundances tend to be significantly larger in the boundary layers as compared to the cooler envelopes. This is possibly the result of ice mantle evaporation and/or sputtering and may also be due to enhanced gas-phase production in the warmer environments. Thus, Rawlings et al. (2004) proposed a general mechanism for molecular enhancement of HCO^+ in a molecular outflow in which carbon atoms, created by the photo-dissociation of newly desorbed CO gas, are photo-ionized and react with H_2O to form HCO^+ .

Chemical fractionation apparently has a major impact on the molecular abundance of the CO isotopes species. In Carolan et al. (2008) larger than expected $^{13}\text{CO} : ^{12}\text{CO}$ ratios, compared with standard galactic values, were found for L483. This is also the case for the three sources studied here with L1527 exhibiting particularly enhanced ^{13}CO emission. The exothermic fractionation reaction leading to the creation of ^{13}CO (Duley & Williams 1984) is



where the zero-point energy difference ΔE is equivalent to a temperature $\Delta E/k$ of 35 K. This mechanism is a likely source for the enhanced abundance observed from our modelling. Alternatively, the enhanced emission from this species could be an excitation effect caused by the scattering of photons from the source by a moderately dense large extended

scattering medium (e.g. Cernicharo & Guelin 1987). Investigation of such an opacity effect would require further MOLLIE modelling of such an external scattering medium and may be appropriate for sources more deeply embedded in extended dense molecular gas. Similar fractionation effects may also be responsible for the apparent lack of correlation between the abundance of C^{18}O and the CO depletion factor.

The abundance of H^{13}CO^+ was constrained in B335 and L1527. The ratio of $^{13}\text{CO}/\text{H}^{13}\text{CO}^+$ in each core is ≈ 2000 though it is slightly higher in L1527. The abundance of ^{13}CO is greatly enhanced in L1527 - by a factor of ~ 80 (compared to a factor of ~ 2 in B335). This indicates that the fractionation effect discussed above for the formation of ^{13}CO is also feeding through to H^{13}CO^+ , which is itself formed from ^{13}CO .

Finally we note again that despite the wide range of line profile appearances, a simple outflow morphology is sufficiently robust for the purpose of analysing the sources. 3D modelling with a code such as MOLLIE enables viewing angle effects to be isolated and reveals the underlying similarities and differences of the sources to be established.

7 SUMMARY AND CONCLUSIONS

We have used a highly simplified physical model of Class 0 protostellar sources, characterized by a spherically symmetric infalling envelope and collimated bipolar outflows - coupled to a 3-D radiative transfer code - to model the line emission spectra from molecular gas surrounding three sources. Physical and chemical parameters were initially constrained from observational data and then refined by the modelling and a best fit chi-squared analysis.

The simplicity of the model was justified on grounds of structure detectability, due to the limited resolution of single dish observations. However, using several different gas species in several transitions observed towards three different sources it was found that this model accurately and self-consistently reproduces the observed spectral line profiles.

The main finding of this study is that, although the three sources we investigate here have dramatically different line profile shapes, we find that once (observationally constrained) infall, depletion and outflow components are introduced, a single morphological model fits all three sources. This verifies the dominance of source morphology in determining line profile shapes. It would be very difficult to fit the data with significantly different physical models, as the detailed structure of the line profiles is largely defined by the physics of the outflow and the envelope. The model and the values of its parameters are essentially defined by empirical constraints. An alternative approach would be to formulate a more detailed theoretical model of the sources and then to attempt to match that with the observations. Such an approach was adopted by Downes & Cabrit (2003) in their hydrodynamic models of jet-driven molecular outflows. From this, they were able to identify a simple intensity-velocity relationship. This was successfully applied, in a modified exponential form, by Lefloch et al. (2012) to fit *Herschel*-HIFI data for five sources. Although this is a different type of modelling to what we have performed - and is applicable to larger scale, higher velocity ($> 10\text{km s}^{-1}$) flows - it should be possible to link consistently the two models.

We find that the principal cause of the source-to-source variations is found to be the difference in the viewing angles; specifically, the angle between the outflow axis and the plane of the sky and *not* the assumptions about the dynamics of the inflow or outflow. This is evident from the large variations in the line profiles that we have successfully modelled as being primarily due to variation of the viewing angle. No variation of any other parameter or combination of parameters can result in such large differences.

The analysis of the multi-transition, spatially resolved line profiles has yielded strong constraints on the chemical and physical parameters of the envelope, outflow and boundary layer of each source. What is remarkable is that the physical parameters for each of the sources, as presented in Tables 3-5, are very similar - the biggest differences between the sources being the abundance ratios of the isotopologues.

We find strong evidence for systemic molecular depletion in all three sources. In addition, we find that

(i) The $\text{C}^{18}\text{O}:\text{C}^{17}\text{O}$ abundance ratio is approximately the same for each of the sources and is consistent with the value found in interstellar clouds (Schöier et al. 2002),

(ii) The abundances of ^{12}CO and ^{13}CO are larger in the bipolar outflow than in the envelope. This is probably a result of thermal evaporation and/or sputtering of the dust ice mantles,

(iii) The ratio of the ^{13}CO abundances in the outflow to that in the envelope is ~ 3 in B335 and ~ 2 in I04166. A much larger value (~ 80) is found for L1527. Our previous analysis for L483 yielded a value of ~ 32 . The ratio for ^{12}CO is ~ 2 for both L1527 and L483. These variations perhaps reflect different degrees of dynamical activity in the sources, and

(iv) As found in L483 (Carolan et al. 2008) there is evidence for ^{13}CO being preferentially enhanced over ^{12}CO in L1527, probably due to chemical fractionation effects.

These studies clearly show the importance of the adoption of realistic morphological/dynamical models of infall/outflow sources, coupled with full 3-D radiative transfer codes in the analysis of star-forming regions. This approach will be essential in the analysis of ALMA data and in focussing on the small-scale structure of the outflows. On these small scales many of our simplifying assumptions (such as that of isothermality) will no longer be applicable. In these situations, the model will need to be modified to include a detailed thermal structure and the effects of more complex morphologies and sub-structure in the outflows.

ACKNOWLEDGMENTS

We thank Eric Keto, Robin Garrod and David Williams for useful discussions and assistance with the observational and modelling work. We also thank an anonymous referee for constructive comments. The James Clerk Maxwell Telescope is operated by the Joint Astronomy Centre on behalf of the Science and Technology Facilities Council of the United Kingdom, the Netherlands Organisation for Scientific Research, and the National Research Council of Canada. MPR acknowledges support from a Science Foundation Ireland Research Frontiers Programme grant (06RFP/PHY051) and from the COST Action CM0805 ‘‘The Chemical Cosmos’’.

REFERENCES

- André P., Ward-Thompson D., Barsony M., 1993, *ApJ*, 406, 122
- Arce H.G., Goodman A. A., 2002, *ApJ*, 575, 911
- Arreaga-García G., Klapp-Escribano J., Gómez-Ramírez F., 2010, *A&A*, 509, A96
- Bachiller R., 1996, *ARA&A*, 34, 111
- Bonner W. B., 1956, *MNRAS*, 116, 351
- Bontemps S., André P., Terebey S., Cabrit S., 1996, *A&A*, 311, 858
- Cabrit S., Goldsmith P. F., Snell R. L., 1988, *ApJ*, 334, 196
- Carolan P. B. 2009, PhD thesis, National University of Ireland Galway
- Carolan P.B. et al., 2009, *MNRAS*, 400, 78
- Carolan P.B., Redman M. P., Keto E., Rawlings J. M. C., 2008, *MNRAS*, 383, 705
- Cernicharo J., Guelin M., 1987, *A&A*, 176, 299
- Chandler C. J., Sargent A. I., 1993, *ApJL*, 414, L29
- Chandrasekhar S., 1967, *An introduction to the study of stellar structure* (New York: Dover, 1967)
- Chen X., Launhardt R., Henning T., 2007, *ApJ*, 669, 1058
- Choi M., Evans II N.J., Gregersen E.M., Wang Y., 1995, *ApJ*, 448, 742
- Downes T.P., Cabrit S., 2003, *A&A*, 403, 135
- Duley W.W., Williams D.A., 1984, *Interstellar Chemistry* (Academic Press)
- Ebert R., 1955, *Zeitschrift fur Astrophysics*, 37, 217
- Elias J.H., 1978, *ApJ*, 224, 857
- Evans II N.J., Lee J.E., Rawlings J.M.C., Choi M., 2005, *ApJ*, 626, 919
- Gao Y., Lou Y.Q., 2010, *MNRAS*, 403, 1919
- Gueth F., Guilloteau S., 1999, *A&A*, 343, 571
- Harvey D.W.A., Wilner D.J., Lada C.J., Myers P.C., Alves J.F., Chen H., 2001, *ApJ*, 563, 903
- Hirano N., Kameya O., Nakayama M., Takakubo K., 1988, *ApJ*, 327, L69
- Hodapp K.W., 1998, *ApJ*, 500, L183
- Huard T.L., Sandell G., Weintraub D.A., 1999, *ApJ*, 526, 833
- Jørgensen J.K. et al., 2007, *ApJ*, 659, 479
- Kenyon S.J., Hartmann L.W., Strom K.M., Strom S.E., 1990, *AJ*, 99, 869
- Kenyon S.J., Whitney B.A., Gomez M., Hartmann L., 1993, *ApJ*, 414, 773
- Keto E., 1990, *ApJ*, 355, 190
- Keto E., Rybicki G.B., Bergin E.A., Plume R., 2004, *ApJ*, 613, 355
- Kramer C., Richer J., Mookerjea B., Alves J., Lada C., 2003, *A&A*, 399, 1073
- Lacy J.H., Knacke R., Geballe T.R., Tokunaga A.T., 1994, *ApJ*, 428, L69
- Lada C.J., Bergin E.A., Alves J.F., Huard T.L., 2003, *ApJ*, 586, 286
- Ladd E.F., Fuller G.A., Deane J.R., 1998, *ApJ*, 495, 871
- Lee C.F., Mundy L.G., Stone J.M., Ostriker E.C., 2002, *ApJ*, 576, 294
- Lefloch B., Cabrit S., Busquet G., Codella C., Ceccarelli C., Pardo J.R., Benedettini M., Lis D.C., Nisini B., 2012, *ApJL*, 757, L25
- Livio M., 2004, *Baltic Astronomy*, 13, 273
- Longmore S.N., Pillai T., Keto E., Zhang Q., Qiu K., 2011, *ApJ*, 726, 97
- MacLeod J.M., Avery L.W., Harris A., 1994, *J.R. Astron. Soc. Can.*, 88, 265
- Mardones D., Myers P.C., Tafalla M., Wilner D.J., Bachiller R., Garay G., 1997, *ApJ*, 489, 719
- Moriarty-Schieven G.H., Snell R.L., 1989, *ApJ*, 338, 952
- Motte F., André P., 2001, *A&A*, 365, 440
- Myers P.C., Bachiller R., Caselli P., Fuller G.A., Mardones D., Tafalla M., Wilner D.J., 1995, *ApJ*, 449, L65
- Nisini B. et al., 1999, *A&A*, 343, 266
- Ohashi N., Hayashi M., Ho P.T.P., Momose M., 1997, *ApJ*, 475, 211
- Ossenkopf V., Henning T., 1994, *A&A*, 291, 943
- Pickett H.M., Poynter R.L., Cohen E.A., Delitsky M.L., Muller J.C.P.H.S.P., 1998, *J. Quant. Spectrosc. & Rad. Transfer*, 60, 883
- Rawlings J.M.C., Redman M.P., Keto E., Williams D.A., 2004, *MNRAS*, 351, 1054
- Redman M.P., Keto E., Rawlings J.M.C., 2006, *MNRAS*, 370, L1
- Redman M.P., Keto E., Rawlings J.M.C., Williams D.A., 2004, *MNRAS*, 352, 1365
- Rybicki G.B., Hummer D.G., 1991, *A&A*, 245, 171
- Saito M., Sunada K., Kawabe R., Kitamura Y., Hirano N., 1999, *ApJ*, 518, 334
- Sandford S.A., Allamandola L.J., 1993, *ApJ*, 417, 815
- Santiago-Garcia J., Tafalla M., Johnstone D., Bachiller R., 2009, *A&A*, 495, 169
- Schnee S., Goodman A., 2005, *ApJ*, 624, 254
- Schöier F.L., Jørgensen J.K., van Dishoeck E.F., Blake G.A., 2002, *A&A*, 390, 1001
- Shirley Y.L., Evans N.J., Rawlings J.M.C., Gregersen E., 2000, *ApJS*, 131, 249
- Shirley Y.L., Evans N.J., Rawlings J.M.C., 2002, *ApJ*, 575, 337
- Shu F.H., 1977, *ApJ*, 214, 488
- Shu F.H., Adams F.C., Lizano S., 1987, *ARA&A*, 25, 23
- Stutz A.M. et al., 2008, *ApJ*, 687, 389
- Tafalla M., Santiago J., Johnstone D., Bachiller R., 2004, *A&A*, 423, L21
- Tamura M., Ohashi N., Hirano N., Itoh Y., Moriarty-Schieven G.H., 1996, *AJ*, 112, 2076
- Tobin J.J., Hartmann L., Calvet N., D'Alessio P., 2008, *ApJ*, 679, 1364
- Tomita Y., Saito T., Ohtani H., 1979, *PASJ*, 31, 407
- Tsamis Y.G., Rawlings J.M.C., Yates J.A., Viti S., 2008, *MNRAS*, 388, 898
- Velusamy T., Kuiper T.B.H., Langer W.D., 1995, *ApJ*, 451, L75
- Ward-Thompson D., Buckley H.D., 2001, *MNRAS*, 327, 955
- Whelan E.T. et al. 2007, *ApJL*, 659, L45
- Wilner D.J., Myers P.C., Mardones D., Tafalla M., 2000, *ApJ*, 544, L69
- Wilson T.L., Rood R.T., 1994, *ARA&A*, 32, 191
- Wiseman J., Wootten A., Zinnecker H., McCaughrean M., 2001, *ApJ*, 550, L87
- Yen H.W., Takakuwa S., Ohashi N., 2010, *ApJ*, 710, 1786
- Yen H.W., Takakuwa S., Ohashi N., 2011, *ApJ*, 742, 57
- Zhou S., Evans II N.J., Wang Y., 1996, *ApJ*, 466, 296
- Zhou S., Evans II N.J., Kömpe C., Walmsley C.M., 1993, *ApJ*, 404, 232

Zhou S., Evans II N.J., Wang Y., Peng R., Lo K., 1994, ApJ, 433, 131

APPENDIX A: ESTIMATING N(H₂) FROM C¹⁸O OBSERVATIONS

The Boltzmann equation describes the level populations in local thermodynamic equilibrium

$$\frac{n_u}{n_l} = \frac{g_u}{g_l} \exp\left(-\frac{h\nu}{kT_{\text{ex}}}\right), \quad (\text{A1})$$

where the n terms are the number density of molecules in the given state, the g terms are the statistical weights and T_{ex} is the excitation temperature. The equation of radiative transfer can be written as

$$T_{\text{A}}^* = \eta_{\text{B}}[J(T_{\text{ex}}) - J(T_{\text{cmb}})][1 - \exp(-\tau)], \quad (\text{A2})$$

where

$$J(T) = \frac{(h\nu/k)}{\exp(h\nu/kT) - 1}. \quad (\text{A3})$$

T_{A}^* is the antenna temperature, η_{B} is the beam efficiency, T_{cmb} is the background temperature, τ is the optical depth of the rotational transition between the upper, u , and the lower, l , states and is given by

$$\tau = (n_l B_{lu} - n_u B_{ul}) \frac{h\nu}{4\pi} \frac{L}{\Delta\nu} \quad (\text{A4})$$

$$= \frac{c^2}{8\pi\nu^2 \Delta\nu} N_l \frac{g_u}{g_l} A_{ul} \left[1 - \exp\left(-\frac{h\nu}{kT_{\text{ex}}}\right)\right]. \quad (\text{A5})$$

Here, B and A are the Einstein coefficients of absorption and emission respectively; L is the path length and so $N = nL$ is the column density; $\Delta\nu \equiv \nu/c\Delta v$ is the line width. Using the Boltzmann equation

$$\tau = \frac{c^2}{8\pi\nu^2 \Delta\nu} N_u A_{ul} \left[\exp\left(\frac{h\nu}{kT_{\text{ex}}}\right) - 1\right], \quad (\text{A6})$$

and using the definition of A_{ul}

$$A_{ul} = \frac{64\pi^4 \nu^3}{3hc^3} \frac{\mu^2 S}{g_u}, \quad (\text{A7})$$

where μ is the permanent dipole moment and S is the line strength gives

$$\frac{N_u}{g_u} = \frac{3h}{8\pi^3} \frac{1}{\mu^2 S} \frac{\tau \Delta\nu}{[\exp(h\nu/kT_{\text{ex}}) - 1]}. \quad (\text{A8})$$

The column density in the transition is related to the total column density of the species by

$$\frac{N_u}{g_u} = \frac{N_{\text{tot}}}{Q(T_{\text{rot}})} \exp\left(-\frac{E_u}{T_{\text{rot}}}\right) \quad (\text{A9})$$

where $Q(T_{\text{rot}})$ is the partition function, E_u is the energy of the upper level and T_{rot} is the rotational temperature, assumed to be the same for all levels. It is usually further assumed that $T_{\text{rot}} = T_{\text{ex}}$ so that

$$N_{\text{tot}} = \frac{3h}{8\pi^3} \frac{Q(T_{\text{ex}})}{\mu^2 S} \tau \Delta\nu \frac{\exp(E_u/kT_{\text{ex}})}{\exp(h\nu/kT_{\text{ex}}) - 1}. \quad (\text{A10})$$

This expression can be used if τ , $\Delta\nu$ and T_{ex} are known.

Alternatively, if the optical depth is small then Equation (A2) becomes

$$T_{\text{A}}^*/\eta_{\text{B}} \simeq [J(T_{\text{ex}}) - J(T_{\text{cmb}})]\tau \quad (\text{A11})$$

and substituting for τ in Equation (A10) and using Equation (A3) gives

$$N_{\text{tot}} = \frac{3k}{8\pi^3 \nu} \frac{Q(T_{\text{ex}})}{\mu^2 S} \frac{J(T_{\text{ex}})}{J(T_{\text{ex}}) - J(T_{\text{cmb}})} \times \exp\left(\frac{E_u}{kT_{\text{ex}}}\right) \int T_{\text{mb}} dv \quad (\text{A12})$$

where we have also used $T_{\text{A}}^* \Delta\nu/\eta_{\text{B}} \simeq \int T_{\text{mb}} dv$, the integrated line intensity. Finally, if $T_{\text{ex}} \gg T_{\text{cmb}}$ this can be simplified further to

$$N_{\text{tot}} = \frac{3k}{8\pi^3 \nu} \frac{Q(T_{\text{ex}})}{\mu^2 S} \exp\left(\frac{E_u}{kT_{\text{ex}}}\right) \int T_{\text{mb}} dv. \quad (\text{A13})$$

If the integrated line strength is measured in km s⁻¹, frequency in GHz, μ in debye then the column density, in CGS units, of an optically thin gas with negligible contribution from the cosmic microwave background is

$$N_{\text{tot}} = 1.67 \times 10^{14} \text{ cm}^{-2} \frac{Q(T_{\text{ex}})}{\nu \mu^2 S} \times \exp\left(\frac{E_u}{kT_{\text{ex}}}\right) \int T_{\text{mb}} dv. \quad (\text{A14})$$

In our models an excitation temperature of 10K is assumed (consistent with the dust temperature) yielding a C¹⁸O rotational partition function of ~ 7.94 . μ is the dipole moment which for C¹⁸O is 0.11079 Debye (Pickett et al. 1998). A conversion factor of 2.07×10^6 is used to convert the C¹⁸O column density into the H₂ column density (Ladd, Fuller & Deane 1998; Lacy et al. 1994; Wilson & Rood 1994).